Hydrogen Evolution Reaction Hot Paper

How to cite: *Angew. Chem. Int. Ed.* **2022,** *61,* e202203850
International Edition: doi.org/10.1002/anie.202203850
German Edition: doi.org/10.1002/ange.202203850

MXene Analogue: A 2D Nitridene Solid Solution for High-Rate Hydrogen Production

*Huanyu Jin[+], Huimin Yu[+], Haobo Li, Kenneth Davey, Taeseup Song, Ungyu Paik, and Shi-Zhang Qiao**

Abstract: Electrocatalysts for high-rate hydrogen evolution reaction (HER) are crucial to clean fuel production. Nitrogen-rich 2D transition metal nitride, designated "nitridene", has shown promising HER performance because of its unique physical/chemical properties. However, its synthesis is hindered by the sluggish growth kinetics. Here for the first time using a catalytic molten-salt method, we facilely synthesized a V–Mo bimetallic nitridene solid solution, $V_{0.2}Mo_{0.8}N_{1.2}$, with tunable electrocatalytic property. The molten-salt synthesis reduces the growth barrier of $V_{0.2}Mo_{0.8}N_{1.2}$ and facilitates V dissolution via a monomer assembly, as confirmed by synchrotron spectroscopy and ex situ electron microscopy. Furthermore, by merging computational simulations, we confirm that the V doping leads to an optimized electronic structure for fast protons coupling to produce hydrogen. These findings offer a quantitative engineering strategy for developing analogues of MXenes for clean energy conversions.

Introduction

The production of high-purity green hydrogen from electrocatalytic water splitting is an acknowledged path to sustainable carbon neutrality.[1] The cost of electrocatalysts is a key determinant for green hydrogen.[2] Most water electrolyzers use conventional noble metal-based electrocatalysts for hydrogen evolution reaction (HER) because of the inherent high activity.[3] However, high price and low reserves of these elements limit large-scale application.[4] Recently, noble metal-free layered transition metal carbides and nitrides, known as MXenes ($M_{n+1}X_nT_x$ M = early transition metals; X = C and/or N; T_x = surface terminations), have been recognized as practically promising HER catalysts.[5] However, pristine two-dimensional (2D) MXenes have an unsatisfactory catalytic performance and inherent oxidative instability.[5c] Complex post-reaction optimizations are often needed to boost overall HER performance.[6] Therefore, new and high-rate 2D MXene-based HER electrocatalysts are essential to the emergent green hydrogen economy.[7]

Nitrogen-rich 2D layered transition metal nitride (TMN) as a MXene analogue has high electrical conductivity, corrosion resistance, and good water splitting stability.[7d,8] We designate this material as "nitridene" because of its structural analogy with MXene. Even though nitridene does not follow the general formula $M_{n+1}X_nT_x$, it has similar physical/chemical properties to MXene, including the 2D layered structure, high electron conductivity and surface terminations.[9] However, pristine nitridene exhibits unsatisfactory HER activity because of a suboptimal hydrogen bonding energy on the atomic-thin crystal surface.[10] Satisfactory activity and corrosion resistance in nitridene are practically difficult to produce simultaneously.

Alloying is considered an "ideal" way to optimize the physical and chemical properties of 2D materials.[11] Manipulating the stoichiometry of the foreign metal atoms within the lattice can tailor the matrix properties for particular applications with new functionality.[12] For example, both electronic and optical properties of 2D transition metal carbide MXene have been tuned by forming solid solutions.[13] The metal-1/metal-2 ratio can be readily controlled within the 2D crystal with alloying.[14] However, alloying foreign metal atoms into a 2D TMN MXene matrix is synthetically challenging because of acknowledged sluggish growth kinetics.[8a,10,15] Additionally, etching and exfoliation are primarily impractical for many TMN-based MXenes because of the high kinetic energy of M–N bonding.[16] For example, the etching process usually destabilize the 2D lattice, leading to the formation of metal oxide instead of 2D

[*] Dr. H. Jin,[+] Dr. H. Li, Prof. K. Davey, Prof. S.-Z. Qiao
School of Chemical Engineering and Advanced Materials,
The University of Adelaide
Adelaide, SA 5005 (Australia)
E-mail: s.qiao@adelaide.edu.au

Dr. H. Jin[+]
Institute for Sustainability, Energy and Resources,
The University of Adelaide
Adelaide, SA 5005 (Australia)

Dr. H. Yu[+]
Future Industries Institute,
University of South Australia, Mawson Lakes Campus
Adelaide, SA 5095 (Australia)

Dr. T. Song, Prof. U. Paik
Department of Energy Engineering,
Hanyang University
Seoul 04763 (Republic of Korea)

[+] These authors contributed equally to this work.

TMNs.[17] For principally these reasons, 2D TMN MXene solid solution has not been synthesized.[17] Therefore, the development of novel 2D nitridiene solid solutions is significant to electrocatalysis and 2D materials chemistry.

Here for the first time, we synthesized a V–Mo bimetallic 2D nitridene solid solution, $V_{0.2}Mo_{0.8}N_{1.2}$, via catalytic molten-salt method. This synthesis ensures a facile growth of nitridene solid solution by lowering the growth barrier of metastable 2D crystals. Additionally, the gas-liquid environment of molten salt provides a monomer assembly, facilitating a substitutional dissolution of V atoms into the $V_{0.2}Mo_{0.8}N_{1.2}$ lattice. The $V_{0.2}Mo_{0.8}N_{1.2}$ exhibited excellent HER activity and stability in acid with a small overpotential of 158 mV at the current density of 10 mA cm^{-2} (η_{10}) together with a long-term HER stability over 100 h. The growth mechanism for $V_{0.2}Mo_{0.8}N_{1.2}$ has been elucidated via advanced synchrotron-based spectroscopy and ex situ aberration-corrected transmission electron microscopy. Synchrotron-based X-ray absorption near edge structure (XANES) and density functional theory (DFT) calculations confirmed that the boosted HER activity of the solid solution originated from the charge redistribution and unique V–N-Mo bonding. The alloyed V atoms provide electrons to the Mo site and ensure an electron-rich active site that promotes hydrogen coupling. We conclude that these findings offer a quantitative strategy for developing MXene analogues for high-rate hydrogen production and will benefit the design of new 2D materials based on earth-abundant transition metals.

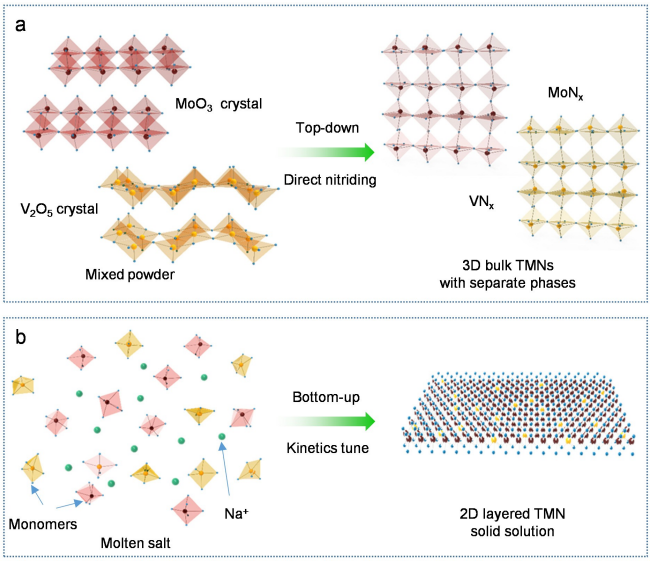

Figure 1. Schematic for the synthesis of a) conventional TMNs and b) 2D $V_{0.2}Mo_{0.8}N_{1.2}$ solid solution through nitridation under NH_3. Direct nitriding of transition metal oxide is a top-down method that facilitates the formation of 3D bulk TMNs. In contrast, the molten-salt environment melts the crystalline precursors into monomers, enabling the growth of a metastable 2D $V_{0.2}Mo_{0.8}N_{1.2}$ solid solution.

Results and Discussion

The 2D layered $V_{0.2}Mo_{0.8}N_{1.2}$ was synthesized via a modified molten-salt method. Precursors of vanadium and molybdenum oxides were mixed with differing V/Mo ratios. Then the metal oxides and Na_2MoO_4 were blended via ball-milling. The $V_{0.2}Mo_{0.8}N_{1.2}$ solid solution was obtained by calcination of metal oxides and alkali salt mixture under NH_3 atmosphere at 650 °C for 2 h. Note that the growth of most metal nitrides is limited by the sluggish kinetics of dissolving N atoms into the metal lattice because of the competition from the recombination of nitrogen molecules and subsequent desorption.[15,18] Therefore, phase separation in the mixture occurs despite the two nitrides being isostructural, Figure 1a. In addition, the stable phases of metal nitrides are usually nitrogen-deficient with 3D atomic structures that limit the diversity of 2D TMNs (Figure S1). Alternatively, the molten-salt method can provide a liquid-gas synthesis, significantly lowering the growth barrier of many 2D materials.[7c,19] As is schematically shown in Figure 1b, the V_2O_5 and MoO_3 are melted into $[VO_5]_{pyramidal}$ and $[MoO_6]_{octahedron}$ prior to nitridation, followed by the growth of 2D nitridene solid solution with the induction of Na ions.[19b,20]

The 2D $V_{0.2}Mo_{0.8}N_{1.2}$ is used in this work as an example to demonstrate the crystal structure and elemental arrangement of the nitridene solid solution. The morphology of $V_{0.2}Mo_{0.8}N_{1.2}$ and other control samples were characterized using scanning electron microscopy (SEM). Both $MoN_{1.2}$ and $V_{0.2}Mo_{0.8}N_{1.2}$ are 2D nanosheets with lateral sizes around 1 μm (Figure S2 and S3). Aberration-corrected high-angle annular dark-field scanning transmission electron microscopy (HAADF-STEM) was used to analyze the V atom arrangement in $V_{0.2}Mo_{0.8}N_{1.2}$ at atomic scale. As a control sample, the single-crystal $MoN_{1.2}$ exhibited a hexagonal structure with an ordered in-plane lattice, Figure 2a. Similarly, $V_{0.2}Mo_{0.8}N_{1.2}$ exhibits hexagonal symmetry of the planes without visible lattice variation. However, significant dark sites were observed as is seen in Figure 2b, which are V atoms because of lower contrast compared with Mo under STEM mode. The nano laminated structure of the two samples can be readily seen in the cross-sectional HAADF-STEM images. The single-layered thickness is about 0.7 nm (Figure S4), and the dissolved V atoms did not change the thickness of the single nanosheet (Figure S5).

The atomic-level energy-dispersive X-ray spectroscopy (EDS) mapping under STEM mode highlights that the V atoms have been successfully alloyed into the $MoN_{1.2}$ lattice, Figure 2c. The elemental distribution demonstrates the existence of O-based terminations on the surface of $V_{0.2}Mo_{0.8}N_{1.2}$. Large-area EDS mapping of $V_{0.2}M_{0.8}N_{1.2}$ confirmed the uniform distribution of V atoms in 2D $V_{0.2}M_{0.8}N_{1.2}$ (Figure S6). Linear electron energy loss spectroscopy (EELS) was used to determine the alloying mode in $V_{0.2}Mo_{0.8}N_{1.2}$, Figure 2d. V L edge spectra were collected in three different positions, Figure 2e. There was no V L edge signal in site 1 and site 3, confirming that Mo atoms occupy the site without V alloying on the top. However, site 2 shows the apparent V L_2 and L_3 signal, Figure 2f. As shown in Figure 2g, the arithmetic average V L edge peak intensity

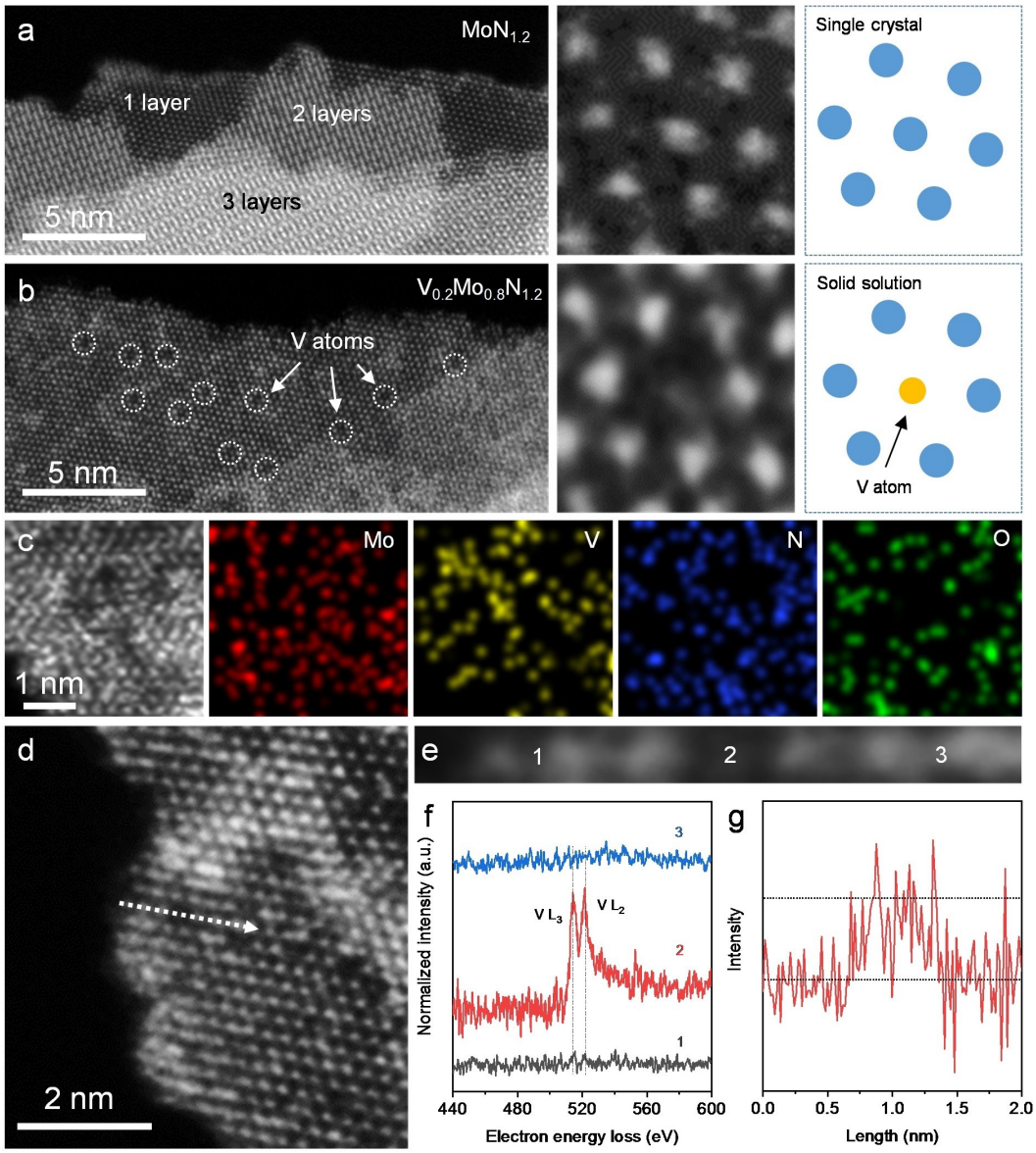

Figure 2. Structural analyses for $V_{0.2}Mo_{0.8}N_{1.2}$ solid solution via electron microscopy. a) HAADF-STEM image of $MoN_{1.2}$ without V doping confirming neat hexagonal crystal lattice. b) HAADF-STEM image of 2D $V_{0.2}Mo_{0.8}N_{1.2}$ solid solution. The white-colour dot-circles highlight V atoms and poor contrast compared with Mo atoms. c) Elemental mapping for $V_{0.2}Mo_{0.8}N_{1.2}$ confirms elements distribution in the lattice. d) and e) HAADF-STEM image of 2D $V_{0.2}Mo_{0.8}N_{1.2}$ highlighting the area of liner EELS. f) High loss EELS spectra for $V_{0.2}Mo_{0.8}N_{1.2}$ corresponding to (d) and (e). g) V L edge intensity for liner EELS analyses.

correlates to the STEM images. These data confirm that the V atoms are alloyed into $V_{0.2}Mo_{0.8}N_{1.2}$ lattice via the substitution of Mo atoms and underscore the 2D unique solid solution structure.

Crystal structure of $V_{0.2}Mo_{0.8}N_{1.2}$ was analyzed via X-ray diffraction (XRD), which confirmed the same crystal structure as for $MoN_{1.2}$, Figure 3a. The peak at 8° confirms the single to few-layer 2D flakes. The redshift for this peak demonstrates a greater interlayer spacing than for $MoN_{1.2}$, indicating the V alloying changes interlayer interaction. Raman spectra for $V_{0.2}Mo_{0.8}N_{1.2}$, $MoN_{1.2}$ and VN_x underscore the effect of solid solution composition on lattice vibrations (Figure S7). The disappearance of several peaks for $V_{0.2}Mo_{0.8}N_{1.2}$ confirms the change of atomic bonding in the lattice compared with $MoN_{1.2}$ and VN_x. Surface-sensitive X-ray photoelectron spectroscopy (XPS) and synchrotron-based XANES measurements were used to determine the bond structure of V in $V_{0.2}Mo_{0.8}N_{1.2}$. The XPS survey scan confirmed the similar chemical composition of $V_{0.2}Mo_{0.8}N_{1.2}$ with $MoN_{1.2}$ (Figure S8a). The Mo/V ratio correlates to the Mo/V ratio in the precursor, confirming that all V atoms in V_2O_5 have been dissolved into the 2D lattice. Both Mo L edge XANES spectra, Figure 3b, and Mo 3d XPS spectra (Figure S8b) showed a lower Mo valence state in

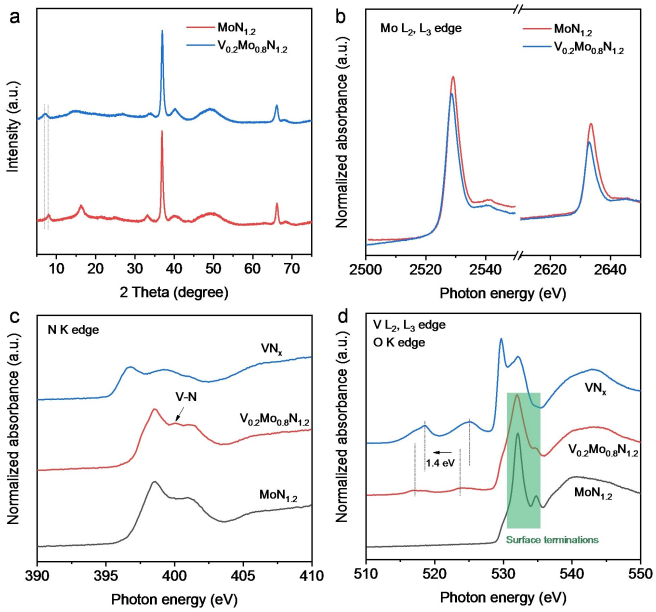

Figure 3. Spectroscopic characterization for $V_{0.2}Mo_{0.8}N_{1.2}$. a) XRD pattern for $V_{0.2}Mo_{0.8}N_{1.2}$ and $MoN_{1.2}$. b) Synchrotron-based Mo L edge XANES spectra for $V_{0.2}Mo_{0.8}N_{1.2}$ and $MoN_{1.2}$. c) Synchrotron-based N K edge XANES spectra and d) V L edge and O K edge XANES spectra for $V_{0.2}Mo_{0.8}N_{1.2}$, VN_x and $MoN_{1.2}$, respectively.

$V_{0.2}Mo_{0.8}N_{1.2}$ compared with $MoN_{1.2}$. As is shown in Figure 3b, the Mo L_2 and L_3 edge of $V_{0.2}Mo_{0.8}N_{1.2}$ negatively shifted 0.6 eV. This energy shift confirms that the alloyed V atoms provide electrons to Mo sites and result in a charge redistribution within the 2D matrix. In the N K edge spectra for $V_{0.2}Mo_{0.8}N_{1.2}$, a new resonance at 400 eV was observed, which attributes to V–N bonding, Figure 3c. The dissolution of V in the lattice is evidenced by the findings from V L edge XANES and XPS. As is shown in Figure 3d, there is an apparent V L edge peak in $V_{0.2}Mo_{0.8}N_{1.2}$ that confirms the existence of V in the sample. The contrasting shape of V L edge confirms that the V–N bonding in $V_{0.2}Mo_{0.8}N_{1.2}$ is different from that in VN_x (Figure S8c). The O K edge spectra for the samples shown in Figure 3d confirm the existence of the O terminations on the surface of 2D nitridene. The invariable O K spectra for $V_{0.2}Mo_{0.8}N_{1.2}$ and $MoN_{1.2}$ underscore that the alloying did not alter the surface termination. Findings from these characterizations confirm the structure of $V_{0.2}Mo_{0.8}N_{1.2}$ in which V atoms are alloyed/doped in $V_{0.2}Mo_{0.8}N_{1.2}$ without phase transformation or separation.

The growth mechanism for the nitridene solid solution was assessed through a series of control experiments. Because the formation of a solid solution needs two isostructural compounds, the lack of 2D layered $VN_{1.2}$ limited the synthesis of $V_{0.2}Mo_{0.8}N_{1.2}$ using conventional approaches. Therefore, the reaction intermediate in our modified method is the critical factor for analyzing the growth of $V_{0.2}Mo_{0.8}N_{1.2}$. A control sample was designed by ceasing synthesis at the early stage to permit determination of reaction intermediates. In detail, the tube-furnace was turned-off immediately when the temperature reached 650 °C. The tube was removed and cooled at room temperature (25 °C) with protection of NH_3. The sample was washed using deionized water and characterized via high-resolution STEM. As is seen in Figure 4a, chain-shaped patterns were observed on the surface of single-layer $V_{0.2}Mo_{0.8}N_{1.2}$. These findings confirm that the growth of nitridene in the molten salt is along the 2D surface by monomer assembling. Additionally, the 2D morphology formation is because of the strong interaction between the in-plane lattice of nitridene and the Na_2MoO_4 salt. The salt interacts with the in-plane facet of $V_{0.2}Mo_{0.8}N_{1.2}$ directly and lowers its activation energy.[10] As a result, the growth of $V_{0.2}Mo_{0.8}N_{1.2}$ along the [110] direction is kinetically favorable and leads to 2D morphology.

An explanation of why the V atoms can be dissolved into the nitridene lattice without 2D layered $VN_{1.2}$ isostructural compounds is as follows: in molten salt, all reactants

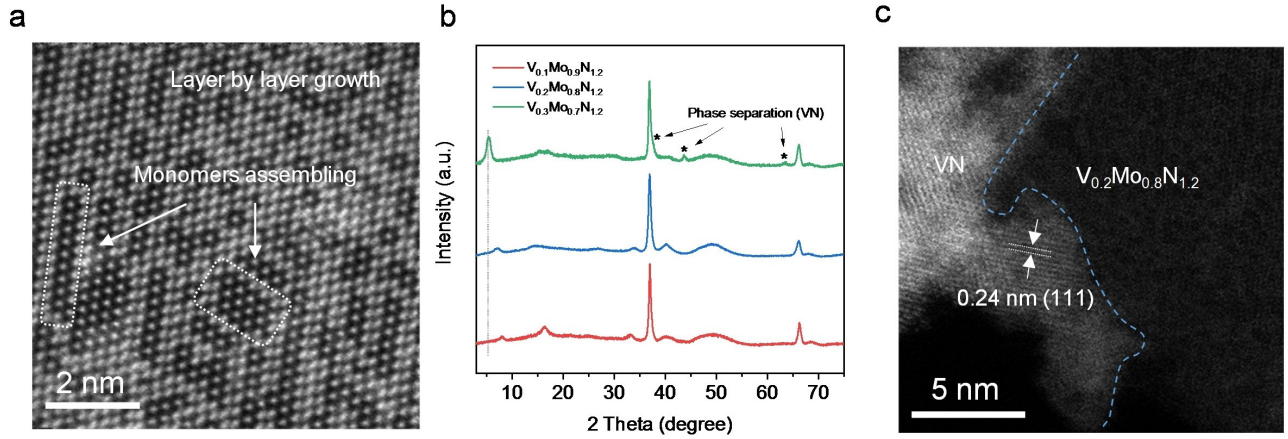

Figure 4. Growth mechanism for 2D $V_{0.2}Mo_{0.8}N_{1.2}$ solid solution. a) HAADF-STEM image of $V_{0.2}Mo_{0.8}N_{1.2}$ at early growth stage. Chain-shape patterns show monomer assembly. b) XRD patterns for V doped $MoN_{1.2}$ with differing V/Mo ratio. c) HAADF-STEM image confirming phase separation of VN on $V_{0.2}Mo_{0.8}N_{1.2}$ surface.

are melted prior to the growth of TMNs, followed by nitridation of the metal oxide monomers. This leads nitride monomers to assemble on the 2D surface. Molten salt can be considered as a supersaturated system where the polymorph with the lowest nucleation barrier forms initially.[21] In the synthesis of $V_{0.2}Mo_{0.8}N_{1.2}$, the growth of the metastable $MoN_{1.2}$ polymorph dominates crystallization Kinetics because of the high activity of metal oxide monomers.[22] The $[VO_5]$ monomer is then linked to $MoN_{1.2}$ atomic chain because of its high concentration. Overall growth kinetics is optimized because of the induction of the alkali metal ions, similar to the growth of other metastable 2D nitridenes.[20,19a,23] Based on combined findings, we conclude that the formation of 2D bimetallic nitridene solid solution consists of three steps: 1) the formation of $[VO_5]_{pyramidal}$ and $[MoO_6]_{octahedron}$ monomers, 2) nitridation of these seeds [Eq. (1)], and; 3) growth of TMN crystals and assembly of $[MoN_x]$ and $[VN_x]$ monomers induced by alkali ions [Eq. (2)]. The Na_2MoO_4 acts as the catalyst during overall synthesis:

$$[MoO_6] + [VO_5] + NH_3 \rightarrow [MoN_x]_{monomer} + [VN_x]_{monomer} + H_2O \quad (1)$$

$$[MoN_x]_{monomer} + [VN_x]_{monomer} + Na^+ + {MoO_4}^{2-} \rightarrow V_{0.2}Mo_{0.8}N_{1.2} + Na_2MoO_4 \quad (2)$$

In the next step, the solubility of the V atoms in the nitridene solid solution was assessed because the V atoms might be expected to have limited solubility due to the lack of isostructural 2D layered vanadium nitride.[12] Two control samples with differing V/Mo ratios denoted as $V_{0.1}Mo_{0.9}N_{1.2}$ and $V_{0.3}Mo_{0.7}N_{1.2}$ were prepared. The solid solution is well-maintained when the alloying level is low, Figure 4b (Figure S9a). However, phase separation occurs when the V/Mo ratio reaches 3:8, Figure 4b. The VN nanoparticles crystallize from the $V_{0.2}Mo_{0.8}N_{1.2}$ lattice because of the oversaturated $[VO_5]$, as is evidenced in the HAADF-STEM image of Figure 4c and Figure S9b. As shown in Figures S10 and S11, the chemical composition did not change however the Mo valence state decreased with the increase of V concentration, confirming that the V atoms provide electrons to Mo. The reaction rate in different growth directions determines the thickness and lateral size of 2D structured materials.[10,21b] With the assistance of alkali metal ions, the growth of 2D $V_{0.2}Mo_{0.8}N_{1.2}$ proceeds along the in-plane direction, as shown in Figure 4a. However, with a significant number of V atoms being dissolved into the lattice, the balance of the crystal is broken, leading to phase separation. In consequence, three design principles emerge to guide the synthesis of 2D $V_{0.2}Mo_{0.8}N_{1.2}$ solid solution: 1) appropriate ratio of alkali metal salt of oxides should be computed carefully to give a stable growth environment, 2) salt must be inactive with ammonia to ensure a catalytic synthesis, and; 3) ratio of foreign atoms, such as V must be less than a specific value to prevent phase separation.

Because of the unique electronic structure, we assessed the electrocatalytic HER activity of $V_{0.2}Mo_{0.8}N_{1.2}$ via electrochemical measurement in 0.5 M H_2SO_4. Figure 5a summarizes the linear sweep voltammetry (LSV) curves for different catalysts. $V_{0.2}Mo_{0.8}N_{1.2}$ exhibited a boosted HER performance, with a η_{10} of 158 mV and a small Tafel slope of 39 mV dec^{-1} (Figure 5b). This is comparable with the Pt/C benchmark of 23 mV and 29 mV dec^{-1}. The Tafel slope of $V_{0.2}Mo_{0.8}N_{1.2}$ is significantly lower than that for $MoN_{1.2}$ and VN_x, demonstrating the optimized electronic structure for HER. In addition, we further investigated the effect of V doping levels on the HER performance of $V_{0.2}Mo_{0.8}N_{1.2}$. As shown in Figure S12, $V_{0.2}Mo_{0.8}N_{1.2}$ shows superior HER performance to the control samples of $V_{0.1}Mo_{0.9}N_{1.2}$ and $V_{0.3}Mo_{0.7}N_{1.2}$. In addition, the Tafel slope of $V_{0.2}Mo_{0.8}N_{1.2}$ reduces to 39 mV dec^{-1} compared to that for $V_{0.1}Mo_{0.9}N_{1.2}$, indicating that the doping process optimizes the Volmer step. However, the phase separation depresses the performance of nitridene solid solution with a Tafel slope of to 50 mV dec^{-1} due to the suboptimal hydrogen adsorption energy of VN nanoparticles. To eliminate the effect of VN_x and $MoN_{1.2}$ interaction, we prepared a control sample of VN_x-$MoN_{1.2}$ heterojunction by mixing VN_x and $MoN_{1.2}$ with the molar ratio of 1:4. As shown in Figure S13, the VN_x-$MoN_{1.2}$ heterojunction shows approximate η_{10} as $MoN_{1.2}$ with a higher Tafel slope of 108 mV dec^{-1}, indicating that the phase interaction between $MoN_{1.2}$ and VN_x is insufficient in facilitating the HER activity. For a comprehensive assessment of the new 2D nitridene solid solution, the η_{10} values and Tafel slope of $V_{0.2}Mo_{0.8}N_{1.2}$ were compared with other 2D MXene-based HER catalysts reported in recent studies, Figure 5c (Table S1).[5c,6a,24] The value of η_{10} and Tafel slope for $V_{0.2}Mo_{0.8}N_{1.2}$ are lower than the corresponding values for most of the reported 2D MXene electrocatalysts because of the unique electronic structure optimized by the dissolved V atoms in the solid solution. Additionally, the electrochemically active surface area (ECSA) of the different samples was assessed to gain insight into HER for $V_{0.2}Mo_{0.8}N_{1.2}$. ECSA is represented by the electrochemical double-layer capacitance (C_{dl}) (Figure S14 and S15). Compared with VN_x, $V_{0.2}Mo_{0.8}N_{1.2}$ has a larger active surface area. However, the ECSA for $V_{0.2}Mo_{0.8}N_{1.2}$ is similar to $MoN_{1.2}$. Therefore, the boosted HER activity is strongly corroborated by its optimized electronic structure rather than the exposed surface area. In addition, DFT calculations were performed to verify the effect of V alloying on the surface charge distribution and HER performance. The average Bader charge of Mo atoms on the surface of V-doped $MoN_{1.2}$ is +0.56, lower than that on the pristine $MoN_{1.2}$ surface of +0.65, confirming the charge transfer between V and Mo. Differential charge density diagram shows that the alloying of V increases the electron density on the catalyst surface (Figure 5d). Reaction free energy diagram further verifies that such an effect of electron accumulation caused by V alloying further enhances the binding strength of the HER reaction intermediate *H at the active sites on the catalyst surface, resulting in higher reactivity (Figure 5e and S16). DFT calculations of charge transfer and free energy match well with the experiments. Thus, we conclude that V alloying weakens the hydrogen bonding energy of the V–N–Mo site and facilitates overall HER.

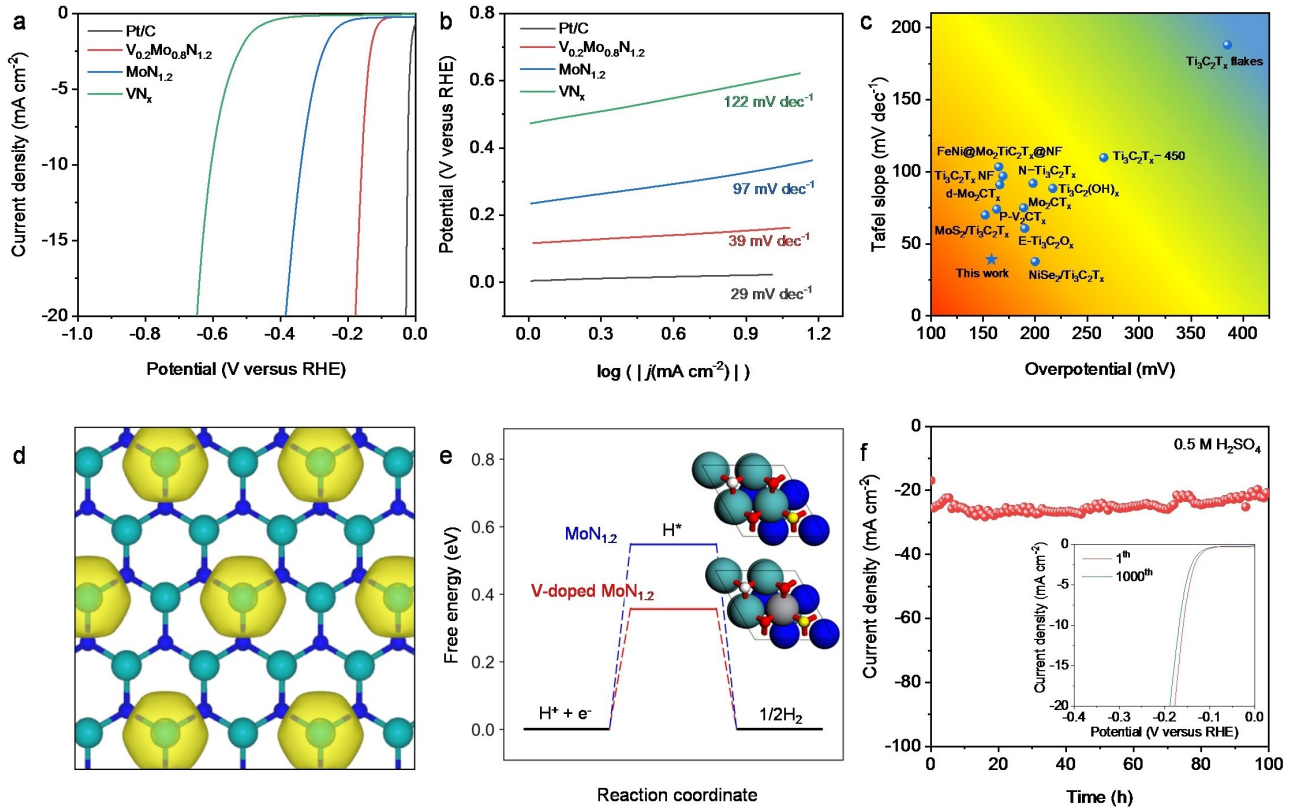

Figure 5. HER performance for 2D $V_{0.2}Mo_{0.8}N_{1.2}$ solid solution and DFT calculations. a) LSV curves and b) corresponding Tafel plots for selected catalysts in Ar-saturated 0.5 M H_2SO_4 solution. Scan rate = 5 mV s^{-1}. c) Comparison of η_{10} and Tafel slope for $V_{0.2}Mo_{0.8}N_{1.2}$ solid solution with reported MXene-based HER catalysts. d) Differential charge density of V-doped $MoN_{1.2}$. The yellow contour represents electron accumulation. The isosurface level is set to be 0.05 e Bohr^{-3}. e) Free energy diagram for HER on $MoN_{1.2}$ (blue) and V-doped Mo_5N_6 (red). The schematic top view of the corresponding atomic structure is shown as the inset. The adsorption site for *H is marked in yellow. Green spheres: Mo; blue spheres: N; grey spheres: V; red spheres: O; white spheres: H. f) Long-term stability of $V_{0.2}Mo_{0.8}N_{1.2}$ solid solution for HER under acid conditions. Inset: LSV curves for $V_{0.2}Mo_{0.8}N_{1.2}$ solid solution at 1st and 1000th cycle.

In addition to activity, the primary practical parameter for MXene-based HER electrocatalyst is stability.[5c] In acid electrolytes, $V_{0.2}Mo_{0.8}N_{1.2}$ exhibits excellent electrocatalytic stability over 100 h (Figure 5f), better than control samples and most MXenes (Figure S17). This electrocatalytic stability demonstrates that the material is active and corrosion resistant in acidic environment. Post-reaction characterizations were further conducted to determine the phase-structure properties for $V_{0.2}Mo_{0.8}N_{1.2}$ after HER. As shown in Figure S18, both the morphology and atom arrangement for $V_{0.2}Mo_{0.8}N_{1.2}$ remain unchanged, demonstrating the stable feature of the crystal structure of nitridene solid solution. In addition, the Mo L edge, V L edge, and O K edge XANES spectra had no visible variation (Figure S19), confirming a stable chemical state for different elements in the 2D lattice. The highly significant stability originates from the unique metal-nitrogen bonding in 2D nitridene solid solution and the inherent anti-corrosive property of 2D TMNs.

Conclusion

In summary, a new MXene analogue, 2D layered $V_{0.2}Mo_{0.8}N_{1.2}$ solid solution, was synthesized for high-rate hydrogen production. Compared with conventional MXenes, the $V_{0.2}Mo_{0.8}N_{1.2}$ exhibited both significant HER activity and long-term electrocatalytic stability. Furthermore, XANES spectra and DFT calculation confirmed that $V_{0.2}Mo_{0.8}N_{1.2}$ has a modified electronic structure, leading to the electron transfer from V to Mo sites for fast protons coupling to produce hydrogen. Findings offer a quantitative strategy for development of MXene analogues for high-rate hydrogen production and clean energy conversions and will be of immediate interest and benefit to the design of new and low-cost 2D materials based on earth-abundant transition metals.

Acknowledgements

This work was financially supported by the Australian Research Council (DP160104866 and FL170100154) and the Korea Institute of Energy Technology Evaluation and

Planning (KETEP), funded by the Ministry of Trade, Industry & Energy (MOTIE) of the Republic of Korea [20203030040030]. H. Jin acknowledges financial support from The University of Adelaide, Future Making Fellowship. XANES measurements were undertaken on the soft X-ray beamline at the Australian Synchrotron. SEM and TEM measurements were conducted at Adelaide Microscopy, the Centre for Advanced Microscopy and Microanalysis. H. Li gratefully acknowledges the Gauss Centre for Supercomputing e.V. (www.gauss-centre.eu) for providing computing time through the John von Neumann Institute for Computing (NIC) on the GCS Supercomputer JUWELS[25] at Jülich Supercomputing Centre (JSC). Open access publishing facilitated by The University of Adelaide, as part of the Wiley - The University of Adelaide agreement via the Council of Australian University Librarians.

Conflict of Interest

The authors declare no conflict of interest.

Data Availability Statement

The data that support the findings of this study are available from the corresponding author upon reasonable request.

Keywords: 2D Nitridene · Catalyst Design · Electrocatalysis · Hydrogen Evolution · MXenes

[1] a) S. Chu, A. Majumdar, *Nature* **2012**, *488*, 294–303; b) T. Wang, L. Tao, X. Zhu, C. Chen, W. Chen, S. Du, Y. Zhou, B. Zhou, D. Wang, C. Xie, P. Long, W. Li, Y. Wang, R. Chen, Y. Zou, X.-Z. Fu, Y. Li, X. Duan, S. Wang, *Nat. Catal.* **2022**, *5*, 66–73; c) *The Future of Hydrogen IENA* **2019**; d) N. van Hulst, *The clean hydrogen future has already begun IEA* **2019**; e) P. Prabhu, V. Jose, J.-M. Lee, *Adv. Funct. Mater.* **2020**, *30*, 1910768.

[2] M. F. Lagadec, A. Grimaud, *Nat. Mater.* **2020**, *19*, 1140–1150.

[3] N. M. Markovic, *Nat. Mater.* **2013**, *12*, 101–102.

[4] a) Z. W. Seh, J. Kibsgaard, C. F. Dickens, I. Chorkendorff, J. K. Nørskov, T. F. Jaramillo, *Science* **2017**, *355*, eaad4998; b) P. Prabhu, J.-M. Lee, *Chem. Soc. Rev.* **2021**, *50*, 6700–6719.

[5] a) B. Anasori, M. R. Lukatskaya, Y. Gogotsi, *Nat. Rev. Mater.* **2017**, *2*, 16098; b) Z. W. Seh, K. D. Fredrickson, B. Anasori, J. Kibsgaard, A. L. Strickler, M. R. Lukatskaya, Y. Gogotsi, T. F. Jaramillo, A. Vojvodic, *ACS Energy Lett.* **2016**, *1*, 589–594; c) K. R. G. Lim, A. D. Handoko, L. R. Johnson, X. Meng, M. Lin, G. S. Subramanian, B. Anasori, Y. Gogotsi, A. Vojvodic, Z. W. Seh, *ACS Nano* **2020**, *14*, 16140–16155.

[6] a) Y. Zhu, J. Sokolowski, X. Song, Y. He, Y. Mei, G. Wu, *Adv. Energy Mater.* **2020**, *10*, 1902844; b) J. Zhang, Y. Zhao, X. Guo, C. Chen, C.-L. Dong, R.-S. Liu, C.-P. Han, Y. Li, Y. Gogotsi, G. Wang, *Nat. Catal.* **2018**, *1*, 985–992.

[7] a) L. Xiu, W. Pei, S. Zhou, Z. Wang, P. Yang, J. Zhao, J. Qiu, *Adv. Funct. Mater.* **2020**, *30*, 1910028; b) X. Wu, Z. Wang, M. Yu, L. Xiu, J. Qiu, *Adv. Mater.* **2017**, *29*, 1607017; c) X. Xiao, H. Wang, W. Bao, P. Urbankowski, L. Yang, Y. Yang, K. Maleski, L. Cui, S. J. L. Billinge, G. Wang, Y. Gogotsi, *Adv. Mater.* **2019**, *31*, 1902393; d) H. Yu, X. Yang, X. Xiao, M. Chen, Q. Zhang, L. Huang, J. Wu, T. Li, S. Chen, L. Song, L. Gu, B. Y. Xia, G. Feng, J. Li, J. Zhou, *Adv. Mater.* **2018**, *30*, 1805655.

[8] a) H. Jin, X. Liu, A. Vasileff, Y. Jiao, Y. Zhao, Y. Zheng, S.-Z. Qiao, *ACS Nano* **2018**, *12*, 12761–12769; b) H. Wang, J. Li, K. Li, Y. Lin, J. Chen, L. Gao, V. Nicolosi, X. Xiao, J.-M. Lee, *Chem. Soc. Rev.* **2021**, *50*, 1354–1390.

[9] H. Jin, L. Li, X. Liu, C. Tang, W. Xu, S. Chen, L. Song, Y. Zheng, S.-Z. Qiao, *Adv. Mater.* **2019**, *31*, 1902709.

[10] H. Jin, Q. Gu, B. Chen, C. Tang, Y. Zheng, H. Zhang, M. Jaroniec, S.-Z. Qiao, *Chem* **2020**, *6*, 2382–2394.

[11] a) H. Jin, X. Wang, C. Tang, A. Vasileff, L. Li, A. Slattery, S.-Z. Qiao, *Adv. Mater.* **2021**, *33*, 2007508; b) H. Wang, L. Ouyang, G. Zou, C. Sun, J. Hu, X. Xiao, L. Gao, *ACS Catal.* **2018**, *8*, 9529–9536; c) L. Wang, Z. Sofer, J. Luxa, M. Pumera, *Adv. Mater. Interfaces* **2015**, *2*, 1500041; d) H. Wang, X. Xiao, S. Liu, C.-L. Chiang, X. Kuai, C.-K. Peng, Y.-C. Lin, X. Meng, J. Zhao, J. Choi, Y.-G. Lin, J.-M. Lee, L. Gao, *J. Am. Chem. Soc.* **2019**, *141*, 18578–18584; e) H. Wang, J. Chen, Y. Lin, X. Wang, J. Li, Y. Li, L. Gao, L. Zhang, D. Chao, X. Xiao, J.-M. Lee, *Adv. Mater.* **2021**, *33*, 2008422; f) Y. Lin, H. Wang, C.-K. Peng, L. Bu, C.-L. Chiang, K. Tian, Y. Zhao, J. Zhao, Y.-G. Lin, J.-M. Lee, L. Gao, *Small* **2020**, *16*, 2002426.

[12] a) C. Tan, X. Cao, X. J. Wu, Q. He, J. Yang, X. Zhang, J. Chen, W. Zhao, S. Han, G. H. Nam, M. Sindoro, H. Zhang, *Chem. Rev.* **2017**, *117*, 6225–6331; b) B. Chen, T. Wang, S. Zhao, J. Tan, N. Zhao, S. P. Jiang, Q. Zhang, G. Zhou, H.-M. Cheng, *Adv. Mater.* **2021**, *33*, 2007090; c) B. Chen, D. Wang, J. Tan, Y. Liu, M. Jiao, B. Liu, N. Zhao, X. Zou, G. Zhou, H.-M. Cheng, *J. Am. Chem. Soc.* **2022**, *144*, 3106–3116.

[13] M. Han, K. Maleski, C. E. Shuck, Y. Yang, J. T. Glazar, A. C. Foucher, K. Hantanasirisakul, A. Sarycheva, N. C. Frey, S. J. May, V. B. Shenoy, E. A. Stach, Y. Gogotsi, *J. Am. Chem. Soc.* **2020**, *142*, 19110–19118.

[14] L. Wang, M. Han, C. E. Shuck, X. Wang, Y. Gogotsi, *Nano Energy* **2021**, *88*, 106308.

[15] W. Sun, C. J. Bartel, E. Arca, S. R. Bauers, B. Matthews, B. Orvañanos, B.-R. Chen, M. F. Toney, L. T. Schelhas, W. Tumas, J. Tate, A. Zakutayev, S. Lany, A. M. Holder, G. Ceder, *Nat. Mater.* **2019**, *18*, 732–739.

[16] S. Venkateshalu, J. Cherusseri, M. Karnan, K. S. Kumar, P. Kollu, M. Sathish, J. Thomas, S. K. Jeong, A. N. Grace, *ACS Omega* **2020**, *5*, 17983–17992.

[17] M. Naguib, M. W. Barsoum, Y. Gogotsi, *Adv. Mater.* **2021**, *33*, 2103393.

[18] F. Song, W. Li, J. Yang, G. Han, P. Liao, Y. Sun, *Nat. Commun.* **2018**, *9*, 4531.

[19] a) X. Xiao, H. Wang, P. Urbankowski, Y. Gogotsi, *Chem. Soc. Rev.* **2018**, *47*, 8744–8765; b) L. Liu, J. Wu, L. Wu, M. Ye, X. Liu, Q. Wang, S. Hou, P. Lu, L. Sun, J. Zheng, L. Xing, L. Gu, X. Jiang, L. Xie, L. Jiao, *Nat. Mater.* **2018**, *17*, 1108–1114.

[20] a) J. Odahara, W. Sun, A. Miura, N. C. Rosero-Navarro, M. Nagao, I. Tanaka, G. Ceder, K. Tadanaga, *ACS Mater. Lett.* **2019**, *1*, 64–70; b) M. S. Sokolikova, C. Mattevi, *Chem. Soc. Rev.* **2020**, *49*, 3952–3980; c) S. Wang, H. Ge, S. Sun, J. Zhang, F. Liu, X. Wen, X. Yu, L. Wang, Y. Zhang, H. Xu, J. C. Neuefeind, Z. Qin, C. Chen, C. Jin, Y. Li, D. He, Y. Zhao, *J. Am. Chem. Soc.* **2015**, *137*, 4815–4822.

[21] a) W. Sun, G. Ceder, *CrystEngComm* **2017**, *19*, 4576–4585; b) Z. Hu, X. Xiao, H. Jin, T. Li, M. Chen, Z. Liang, Z. Guo, J. Li, J. Wan, L. Huang, Y. Zhang, G. Feng, J. Zhou, *Nat. Commun.* **2017**, *8*, 15630.

[22] a) J. Zhou, J. Lin, X. Huang, Y. Zhou, Y. Chen, J. Xia, H. Wang, Y. Xie, H. Yu, J. Lei, D. Wu, F. Liu, Q. Fu, Q. Zeng, C.-H. Hsu, C. Yang, L. Lu, T. Yu, Z. Shen, H. Lin, B. I. Yakobson, Q. Liu, K. Suenaga, G. Liu, Z. Liu, *Nature* **2018**, *556*, 355–359; b) C. Xu, L. Wang, Z. Liu, L. Chen, J. Guo, N.

Kang, X. L. Ma, H. M. Cheng, W. Ren, *Nat. Mater.* **2015**, *14*, 1135–1141; c) M. Zeng, Y. Xiao, J. Liu, K. Yang, L. Fu, *Chem. Rev.* **2018**, *118*, 6236–6296.

[23] a) Y.-R. Zheng, P. Wu, M.-R. Gao, X.-L. Zhang, F.-Y. Gao, H.-X. Ju, R. Wu, Q. Gao, R. You, W.-X. Huang, S.-J. Liu, S.-W. Hu, J. Zhu, Z. Li, S.-H. Yu, *Nat. Commun.* **2018**, *9*, 2533; b) X. Xiao, H. Yu, H. Jin, M. Wu, Y. Fang, J. Sun, Z. Hu, T. Li, J. Wu, L. Huang, Y. Gogotsi, J. Zhou, *ACS Nano* **2017**, *11*, 2180–2186; c) D. Voiry, A. Mohite, M. Chhowalla, *Chem. Soc. Rev.* **2015**, *44*, 2702–2712.

[24] a) Y. Jiang, T. Sun, X. Xie, W. Jiang, J. Li, B. Tian, C. Su, *ChemSusChem* **2019**, *12*, 1368–1373; b) Y. Yoon, A. P. Tiwari, M. Choi, T. G. Novak, W. Song, H. Chang, T. Zyung, S. S. Lee, S. Jeon, K.-S. An, *Adv. Funct. Mater.* **2019**, *29*, 1903443; c) J. Liu, Y. Liu, D. Xu, Y. Zhu, W. Peng, Y. Li, F. Zhang, X. Fan, *Appl. Catal. B* **2019**, *241*, 89–94.

[25] Jülich Supercomputing Centre. JUWELS Cluster and Booster: Exascale Pathfinder with Modular Supercomputing Architecture at Juelich Supercomputing Centre. *Journal of large-scale research facilities* **2021**, *7*, A183, https://doi.org/10.17815/jlsrf-17817-17183.

Manuscript received: March 15, 2022
Accepted manuscript online: April 19, 2022
Version of record online: May 3, 2022